SCIENCE CHINA Materials **ARTICLES**

mater.scichina.com link.springer.com

Sci China Mater 2025, 68(10): 3703–3714
https://doi.org/10.1007/s40843-025-3489-5

Low-power plasmonic SiC nanowire network-based artificial photo-synaptic device for musical classification neural network systems

Mi Chen[1], Guodong Wei[1*], Shuai Yuan[1,3], Ying Li[2], Pan Wang[1], Ying Su[1], Liping Ding[1], Ruihong Wang[1] and Guozhen Shen[2*]

ABSTRACT The rapid development of artificial intelligence and the Internet of Things has generated an urgent demand for brain-inspired computing systems characterized by high parallel processing capabilities. However, the power consumption of most reported artificial synaptic devices remains substantially higher than that of their biological counterparts, which operate at the femtojoule (fJ) level per synaptic event. To this end, this research aims to develop ultralow-power silicon carbide (SiC) plasmonic nanowire network (NWN)-based artificial synaptic devices for using in musical classification neural network system. By leveraging the neural network-like physical architecture of the NWN and the alteration of conductance states at NW-NW junctions, the SiC/SiO$_2$@Ag NWN devices successfully emulate both ultraviolet (UV) visual and electrical synaptic functions under both externally biased electric field modulation mode and zero-bias photoexcitation mode conditions. Furthermore, due to the confinement effects of one-dimensional nanomaterials and the localized surface plasmon resonance (LSPR) induced by Ag nanoparticles, these devices exhibit substantial synaptic responses at ultra-low currents with minimal power consumption. With its low power consumption, the SiC/SiO$_2$@Ag NWN synapses exhibit superior performance in simulating music classification recognition, achieving an accuracy exceeding 95% within 20 epochs. Notably, the innovative SiC NWN structure ensures robust synaptic performance and high precision in neural network computations. This advancement has the potential to drive the development of novel computing architectures, such as spiking neural networks (SNNs), which more closely mimic the operational principles of biological neural networks, thereby facilitating enhanced music information processing.

Keywords: SiC nanowire network, artificial synapse, LSPR effect, musical classification, low power consumption

INTRODUCTION

Neuromorphic devices are designed to simulate the functionality of fundamental biological information processing units, enabling adaptive and efficient hardware-based information processing that overcomes the limitations inherent in traditional von Neumann architectures [1–3]. Within brain-inspired computing systems, these devices mimic both the structural and operational mechanisms of biological neural systems, thus providing robust hardware support for complex neural network computations while significantly reducing power consumption [4,5]. Based on this, a variety of neuromorphic devices have been extensively validated as hardware accelerators for artificial neural networks (ANN) across a broad spectrum of advanced artificial intelligence (AI) applications, including image recognition [6], voice recognition [7], motion detection and recognition [8], and edge learning [9]. Among these applications, the challenge of audio recognition and classification, particularly with music signals, is especially pronounced due to its inherent complexity. Music as a dynamic and intricate temporal signal, encompasses diverse elements such as human language and vocal characteristics, making its analysis particularly demanding.

Synaptic devices, designed to mimic biological synapses, can be regarded as the foundational units of perceiving and processing information for developing neuromorphic devices, which offer substantial advantages in music classification by enhancing energy efficiency, accelerating processing speed, optimizing data storage, improving scalability, and increasing robustness [10–12]. Moreover, they facilitate the development of novel computer architectures necessary for sophisticated music signal processing. Reducing the synaptic scale to the nanometer level not only facilitates the miniaturization, integration, and the energy efficiency of synaptic devices but also promotes the development of novel materials and systems with unique synaptic properties. Extensive research has demonstrated that one-dimensional nanostructures are ideal building blocks for optoelectronic synaptic devices, fully meeting the multifunctionality and low-power requirements of future neuromorphic systems [6,13–15]. Inspired by the intricate connectivity of neurons in the human brain, which is interconnected through multiple pathways rather than single lines, constructing a self-assembled one-dimensional nanowire network (NWN) with storage capabilities, fault tolerance, and adaptability has become a prominent research area [16,17]. Loeffler *et al.* [18] utilized graph theory to validate that the cluster electrical responses generated by complex NW networks closely resemble the structure-function relationship observed in biological neural networks. These networks exhibit collective dynamics similar to brain functions, including phase transitions,

---

[1] Xi'an Key Laboratory of Compound Semiconductor Materials and Devices, School of Physics and Information Science, Shaanxi University of Science and Technology, Xi'an 710021, China
[2] School of Integrated Circuits and Electronics, Beijing Institute of Technology, Beijing 100081, China
[3] School of Physics and Electrical Engineering, Kashi University, Kashi 844006, China
[*] Corresponding author (email: wgd588@163.com; gzshen@bit.edu.cn)

switch synchronization, and avalanche criticality [17,19]. This finding establishes a theoretical foundation for using NW networks as brain-like neural networks to achieve brain-computing functionalities. Within such networks, altering the spatial and temporal characteristics of input signals via electrode positioning and varying transmission amplitudes can create new electrical pathways, mimicking the biological synaptic learning process.

In the process of commercialization, one of the most challenges in this field is to develop highly integrated synaptic device arrays utilizing conventional semiconductor technology. Among these semiconducting materials, the third-generation semiconductor material SiC can support the growth of a high-quality silicon oxide layer on its surface, which is compatible with the traditional semiconductor Si processes, suggesting that SiC is very suitable for fabricating highly integrated synaptic devices on the wafer scale [20]. Synaptic devices based on SiC have attracted more and more attention due to their ability to simulate a variety of biological synaptic functions with power consumption in the fJ order. These devices also exhibit exceptional stability in simulating visual functions and memory learning functions [6,21,22]. However, according to our group's research findings, synaptic devices based on pure SiC NWNs require additional driving voltage to achieve visual synaptic functionality in response to space light stimulation. This not only creates additional power consumption but also affects network performance due to changes in switching behavior. To address the issue of high energy consumption and realize externally biased electric field modulation mode visual synaptic functionality, this study investigated the application potential of SiC NWNs in music classification neural devices by designing a two-terminal artificial synapse device based on $SiC/SiO_2@Ag$ NWNs. The device demonstrates excellent synaptic plasticity under both electrical pulses and ultraviolet (UV) illumination. By leveraging the superior photoelectric properties of SiC NWNs and the localized surface plasmon resonance (LSPR) effect of Ag nanoparticles (NPs), the device can emulate visual synaptic functionality with significantly reduced power consumption under both externally biased electric field modulation mode and zero-bias photoexcitation mode conditions. Benefiting from the superior computational power, the $SiC/SiO_2@Ag$ NWs synapses can have an excellent performance in simulating music classification recognition with over 95% accuracy in only 20 epochs. This level of accuracy and efficiency in music classification not only highlights the potential of these devices in real-world applications but also overcomes the problems of power consumption and integration in synaptic devices, underscoring their importance in advancing the state-of-the-art in neuromorphic computing.

EXPERIMENTAL SECTION

Materials

The chemical reagents employed, including silver nitrate, acetone, and isopropyl alcohol, were all of analytical grade and were procured from Beijing Chemical Plant Co., Ltd. (China). The SiC NW aerogels with an average NW length surpassing 100 μm were synthesized via a cost-effective carbothermal reduction method; detailed procedures were documented in prior literature references [23,24]. Commercially available samples, prepared by our research group, can be obtained from Fujian Zhongwei Semiconductor Materials Co., Ltd.

Synthesize $SiC/SiO_2@Ag$ NWs

The detailed experimental procedure can be found in the reference [25]. In a typical experiment: 40 mg of etched SiC NWs were mixed with a certain amount of $AgNO_3$ powder in a sealable quartz tube. The tube was then evacuated and sealed using a hydrogen-oxygen flame welding machine, ensuring the material in a vacuum environment. Subsequently, the sealed quartz tube was heated in a muffle furnace at 10 °C/min until it reached 1000 °C where it was maintained for 1 h before being naturally cooled to room temperature. Finally, the sample was annealed at 500 °C to form $SiC/SiO_2@Ag$ NWs.

Fabrication of the synaptic device

$SiC/SiO_2@Ag$ NWs (5 mg) were weighed and added to 50 mL isopropyl alcohol to form a uniformly dispersed solution under ultrasonic treatment (ultrasonic power 800 W, 30 min). The resulting suspension was then subjected to vacuum filtration through a 0.22 μm pore size aqueous filter membrane to form a $SiC/SiO_2@Ag$ NWN. Following filtration, the film was dried at 60 °C. Subsequently, the $SiC/SiO_2@Ag$ NWs film was transferred onto the conductive surface of indium tin oxide (ITO) glass with the $SiC/SiO_2@Ag$ NWN side facing the ITO. The supporting filter membrane was then dissolved using an acetone solution. The $SiC/SiO_2@Ag$ NWs film was retained on the ITO substrate and dried again at 60 °C. Then, a silver electrode array with an electrode spacing of 10 μm was fabricated on $ITO/SiC/SiO_2@Ag$ NWs thin films by vacuum thermal evaporation. Finally, the $SiC/SiO_2@Ag$ NWN synaptic devices were positioned on the probe table for synaptic performance testing.

Measurement and characterization

The surface micromorphologies and elemental analysis and crystal structure of $SiC/SiO_2@Ag$ NWs were investigated by field emission scanning electron microscope (FESEM, S-4800, Hitachi, Japan), transmission electron microscope (TEM, FEI Tecnai G2, USA) and X-ray diffraction (XRD, Smart Lab 9 kW, Japan), respectively. The electrical performance analyses of $SiC/SiO_2@Ag$ synaptic device were recorded using a semiconductor characterization system (Keithley 4200 CSC). The light intensity was measured with the CEL-NP2000 power meter. The data of the $SiC/SiO_2@Ag$ synaptic device under optical and electrical stimulations are collected by the 30 MHz oscilloscope (Rigol DG1032) and Keithley 4200 CSC.

RESULTS AND DISCUSSION

$SiC/SiO_2@Ag$ NWs device structure

A typical artificial synaptic device, featuring a two-terminal structure analogous to biological synapses, has been developed using $SiC/SiO_2@Ag$ NWNs. It consists of a top Ag electrode, a $SiC/SiO_2@Ag$ NWN memristor functional layer, and a bottom ITO electrode (Fig. 1a, left). The top Ag electrode simulates the presynaptic membrane and is fabricated using a rectangular array mask plate through vacuum thermal evaporation. The $SiC/SiO_2@Ag$ NWN film serves as the neurotransmitter medium, prepared via a rapid vacuum filtration method, and subsequently transferred onto the surface of ITO glass, which simulates the postsynaptic membrane. Due to its highly similar two-terminal structure and working mechanism to biological synapses, the $SiC/SiO_2@Ag$ NWN-based devices can exhibit biological synaptic behavior in both electrical and optical spike modulation

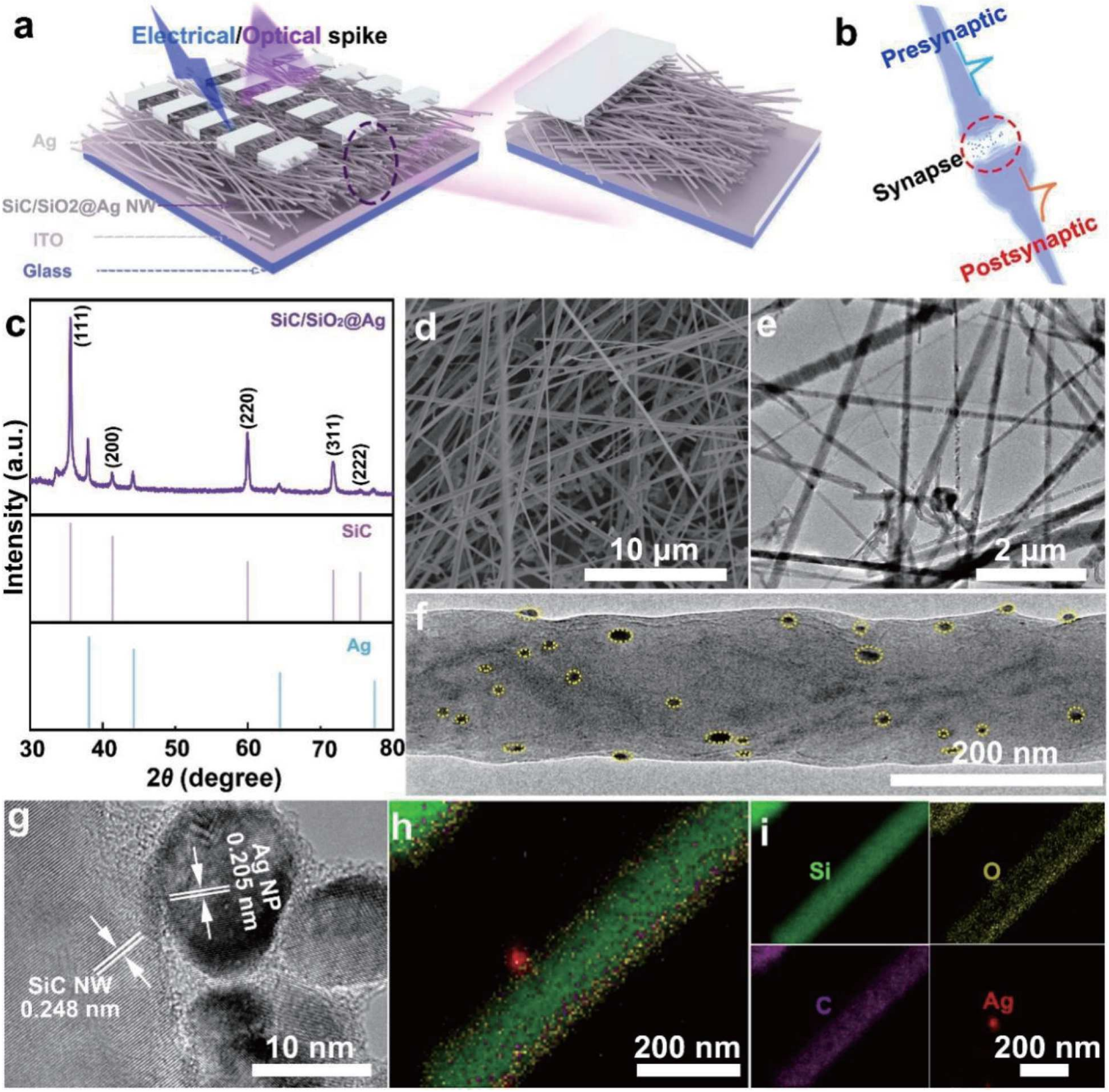

Figure 1 (a) Schematic illustration of the SiC/SiO$_2$@Ag NWN artificial synapse stimulated by electrical or optical spike. The left image depicts the structure of the SiC/SiO$_2$@Ag NW artificial synapse array, while the right image shows the single SiC/SiO$_2$@Ag NW artificial synapse device. (b) Schematic diagram of a typical biological synapse. (c) XRD pattern of the SiC/SiO$_2$@Ag NWNs. (d) Typical SEM image of the SiC/SiO$_2$@Ag NWN film. (e) TEM image of the SiC/SiO$_2$@Ag NWN node, and (f) the diameter distribution of SiC/SiO$_2$@Ag NW. (g) HRTEM image of SiC/SiO$_2$@Ag NW. (h, i) EDS mapping photos of SiC/SiO$_2$@Ag NW.

with externally biased electric field modulation mode and zero-bias photoexcitation mode, as shown in Fig. 1a. Electrical and optical signals are processed within the device in a manner analogous to biological synapses with the current through the NW film corresponding to presynaptic input spikes and postsynaptic current (PSC) in bio-synapses (Fig. 1b). The composition of SiC/SiO$_2$@Ag NWN film was ascertained by XRD. The diffraction peaks clearly demonstrate the Ag phase (JCPSD Card No. 04-0783) and 3C-SiC phase (JCPSD Card No. 29-1129), and the sharp and intense peaks indicate excellent crystallinity of both SiC and Ag (Fig. 1c) . SEM images exhibit the averaged length of NWs exceeding 100 μm (Fig. 1d and Fig. S1). Notably, these ultra-long SiC NWs with randomly interwoven structures significantly enhance the formation of a robust NWN characterized by superior structural stability (Fig. S1). The integration of these elongated, highly crystalline NW serves as an ideal electron channel, thereby facilitating efficient carrier transport and contributing to the development of highly stable, high-performance, and flexible NW networks. TEM images exhibit the interconnection between NWs, forming numerous nodes similar to synaptic junctions in neural networks (Fig. 1e). Single NW analysis reveals a diameter of approximately 150 nm anchored with numerous NPs on the surface (Fig. 1f). The NPs are further analyzed using high-resolution TEM (HRTEM), clearly showing that the SiC NW and NPs exhibit high crystal quality with well-ordered periodic arrangements. Specifically, the interplanar spacing is measured at 2.48 Å along the (111) direction of SiC and 2.05 Å along the (200) direction of Ag

(Fig. 1g), confirming their single-crystal nature and the presence of Ag NPs [26,27]. The energy dispersive spectrometer (EDS) (Fig. 1h, i) elements mappings show the distribution of Si, O, C and Ag elements, further confirming that Ag nanoparticles are loaded on the surface of SiC NW. Aberration-corrected TEM (AC-TEM, Fig. S2a) was used to further characterize the crystal structure of the material following long-term storage. The result demonstrates that the SiC nanowires exhibit well-defined and orderly lattice fringes with negligible defects. The Ag NPs exhibit no apparent signs of oxidation-induced volume expansion or surface roughening even after one year of ambient storage. EDS mappings (Fig. S2b–f) demonstrate the spatial distribution of Si, C, Ag, and O elements. These findings suggest that Ag atoms can diffuse from surface nanoparticles into the nanowire interior due to high-temperature synthesis conditions. Furthermore, no oxygen enrichment around Ag NPs was observed.

Externally biased electric field modulation mode light-modulated visual synapse

The SiC/SiO_2@Ag NWN artificial synapse device, which emulates the operational mechanism of biosynapses, has successfully replicated the function of the visual nerve system, a crucial component for human information acquisition. Under a bias voltage of 1 V (externally biased electric field modulation mode), the SiC/SiO_2@Ag NWN device undergoes optical stimulation, and the resulting photoresponsive data are processed using typical neuromorphic approaches, thereby achieving outcomes that accurately simulate synaptic function as illustrated in Fig. 2a. Short-term plasticity (STP), as the fundamental characteristic of biological synapses in neuroscience, plays a crucial role in biological cognition and learning processes. To determine whether the SiC/SiO_2@Ag NWN device can replicate this functionality, we utilized 365 nm pulsed light to stimulate the device. Upon application of a presynaptic light spike, an excitatory post-synaptic current (EPSC) can be elicited [28,29]. As a prototypical form of STP, paired-pulse facilitation (PPF) represents a crucial phenomenon in neuroscience for assessing the impact of two consecutive stimuli on synaptic strength. The EPSC elicited by the second presynaptic spike exhibits a significantly greater magnitude compared to that elicited by the first spike when a pair of light spikes (365 nm, 326 mW/cm^2, pulse width = 200 ms) is applied to the SiC/SiO_2@Ag NWN device (Fig. 2b, inset). This observation aligns with the response characteristics of biological synapses under similar conditions. Typically, the promotion effect is quantified using the PPF index ($A_2/A_1 \times 100\%$), where A_1 and A_2 represent the amplitudes of photo-responsive currents evoked by the first and second light pulses, respectively. The magnitude of PPF induced by the second light pulse is affected by the temporal interval between the stimuli. As the inter-pulse interval (Δt) increases, the promotion effect diminishes, leading to a reduction in synaptic weight modulation (Fig. 2b) [30–32]. Additionally, the PPF indexes can be derived by fitting the double-exponential function $y = 1+C_1\exp(-\Delta t/\tau_1)+C_2\exp(-\Delta t/\tau_2)$, where Δt represents the time interval between two consecutive light pulses, C_1 and C_2 denote the magnitudes of facilitation, and τ_1 and τ_2 correspond to the fast and slow decay times of the exponential function. The fitting results reveal that τ_1 and τ_2 are 0.52 and 1.99 s, respectively (Fig. 2b).

In the biological nervous system, the EPSC can be potentiated in response to intensified external stimuli. The synapse response can vary in magnitude depending on the duration of the stimulus. As depicted in Fig. 2c, the EPSC exhibits a gradual increase from 2.4 to 5.5 pA in response to light pulses of varying durations (365 nm, 326 mW/cm^2, pulse width ranging from 200 to 700 ms), and this phenomenon is known as spike-duration-dependent plasticity (SDDP). Here, the SiC/SiO_2@Ag NWN device effectively mimics the functionality of visual synapses under an externally biased electric field modulation mode state, with minimal power consumption due to its low current draw. In general, the energy consumption of a single synaptic event can be calculated by the following formula: $\int_{t_2}^{t_1} V \cdot I(x)\mathrm{d}x$, where t_1 and t_2 are the time when the stimulus conditions start and stop, V is the operating voltage, and I is the response current of the synaptic device [14,33]. Analysis of the power usage of the SiC/SiO_2@Ag NWN device under different durations of light pulse stimulation reveals that it consumes only 0.218 pJ during a 200 ms pulsed light stimulation. The power consumption increases incrementally with the duration of stimulation, reaching a peak of 1.965 pJ. This energy consumption closely mirrors that observed in human brain synapses, thereby enabling the SiC/SiO_2@Ag NWN device to simulate low-power artificial visual synapses. To understand the crystallographic structure of Ag NPs loaded onto SiC/SiO_2 core-shell NWs, the cross-sectional crystal structure depicted in Fig. 2d, reveals a core composed of 3C-SiC, a SiO_2 shell, and Ag nanoparticles. This configuration exploits the robust crystalline structure of 3C-SiC, which is a cubic SiC variant known for its superior physical and chemical properties. In both SiC and SiO_2 structures, each Si cation is surrounded by a tetrahedron (Td symmetry) of four C and O anions, respectively. Under high-pressure nitrogen oxide gas and a temperature of 1000 °C, Si–O bonds form, resulting in the growth of a SiO_2 shell encapsulating the SiC core. By leveraging electrostatic adsorption of O anions, Ag nanoparticles are anchored onto the surface of SiC/SiO_2 core-shell NWs via Ag–O bonds, as demonstrated in studies where Ag@SiO_2 nanoparticles exhibit enhanced properties such as surface-enhanced Raman scattering and fluorescence [34]. To conduct a comprehensive analysis of internal photoelectron transport and photoresponse mechanism within the device, a band model for the SiC/SiO_2@Ag NW heterojunction was established. Given the higher work function of Ag NPs (5.3 eV) compared to SiC (4.5–5 eV), the Fermi level of Ag nanoparticles is lower than that of SiC, as illustrated in Fig. 2e$_1$. Upon formation of the heterojunction, electrons migrate from the higher Fermi level of SiC to the lower Fermi level of Ag until equilibrium is reached, leaving positively charged ions near the SiC surface and creating a built-in electric field directed from SiC toward the interface. At the interface of SiC, upward band bending is observed in Fig. 2e$_2$. When an external electric field is applied in opposition to the built-in electric field (Fig. 2e$_3$, e$_4$), the total energy bands of SiC shift upward, gradually reducing the degree of upward bending and decreasing the potential barrier height. Especially, when the applied voltage (V_R) exceeds the built-in potential barrier (V_D) (Fig. 2e$_4$), the bending direction of the SiC energy band at the interface reverses, transitioning from upward to downward. This change further facilitates electron tunneling from SiC to Ag NPs. Therefore, the externally applied electric field enhances both the tunneling effect and the separation of photocarriers, leading to an increase

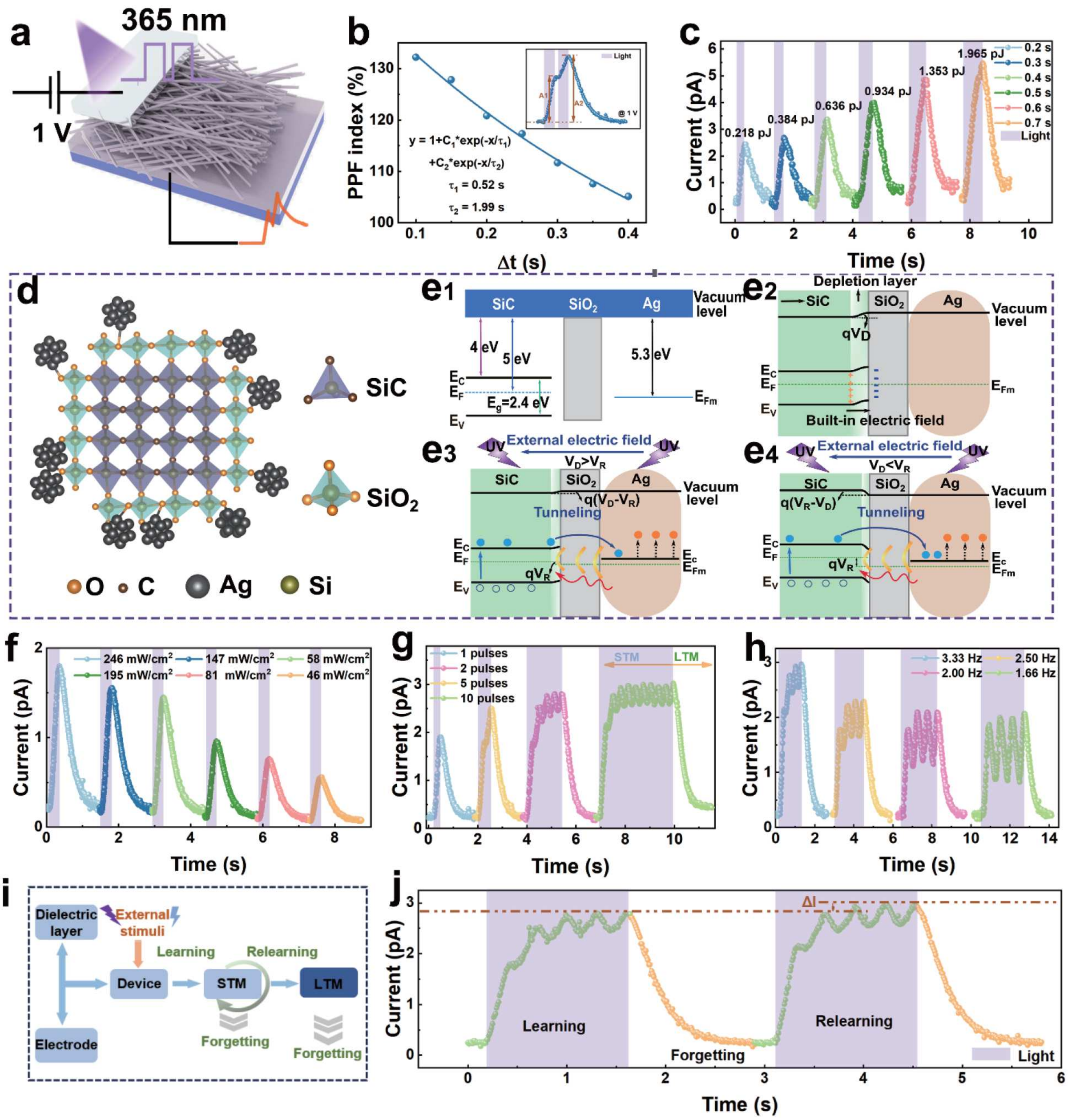

Figure 2 (a) Schematic diagram of the device's externally biased electric field modulation photoexcitation mode. (b) PPF index as a function of the time interval between two light pulses: simulation test of device dissimilation during double-pulse operation. (c) Device power consumption under 365 nm light pulses with varying pulse widths. (d) Atomic model of the SiC/SiO$_2$@Ag NW core-shell structure. (e) Energy band alignment diagram for SiC, SiO$_2$, and Ag (e$_1$) before and (e$_2$) after contact and schematic diagram of the SiC/SiO$_2$@Ag heterojunction under 365 nm UV illumination and an external electric field in the (e$_3$, e$_4$) opposite direction to the built-in electric field. Device response to 365 nm light pulses with varying parameters: (f) power densities, (g) pulse numbers, and (h) frequency tested 10 times. (i) Schematic diagram of device learning and memory behavior. (j) Device's "Learning-Forgetting-Relearning-Forgetting" behavior under light stimulation.

in photocurrent and extended relaxation time under the influence of the external field.

The synaptic response to different stimulus intensities is also modulated by the intensity of the stimuli, a phenomenon known as spike-power-dependent plasticity (SPDP), which refers to transient modifications in synaptic activation responses. When optical pulses with different power density (ranging from 46 to 246 mW/cm^2) are applied to the SiC/SiO$_2$@Ag NW artificial synaptic device, there is a corresponding increase in EPSC (from 0.5 to 1.8 pA), as shown in Fig. 2f. Increasing the number of stimuli can significantly elevate the degree of synaptic connectivity. As the number of light pulses increases (365 nm, 326 mW/cm^2, 200 ms pulse width, 100 ms pulse interval), the EPSC produced by the synapse rises, suggesting an enhanced synaptic memory level due to increased stimulation. The current decay curve in an artificial synapse exhibits similarities to the forgetting curve observed in the human brain. With a tenfold increase in consecutive spikes, there is a significant extension in memory duration. After a single stimulation, the retention time is only 400 ms; however, it can extend to 900 ms after ten stimulations (Fig. 2g).

The frequency of stimulation is a critical determinant of synaptic strength, as it influences synaptic plasticity, which is essential for learning and memory processes. Spike-rate-dependent plasticity (SRDP) refers to the persistent modification of synaptic reactivity in response to repeated synaptic activation. As the presynaptic stimulation frequency increases, the EPSC also tends to increase, consistent with the fundamental properties of biological synapses. When continuous light pulses with varying pulse frequencies (365 nm, 326 mW/cm^2, frequency from 1.66 to 3.33 Hz) are applied to the device over ten repetitions, a gradual decline in EPSC is observed (Fig. 2h). Sensory organs receive external stimuli, which are then processed and recorded by the brain through chemical or physiological mechanisms. Memory formation typically involves the process of learning, forgetting, and relearning. Fig. 2i illustrates these processes in a SiC/SiO$_2$@Ag NWN-based artificial synaptic device stimulated by 365 nm UV light. Conversely, the synaptic device can exhibit heightened responsiveness to high frequency stimulation. Therefore, various modulation methods can alter the memory state of synapses from short-term memory (STM) to long-term memory (LTM) by intensifying the stimulus [35,36]. Moreover, the SiC/SiO$_2$@Ag NWN artificial synaptic devices have successfully replicated the "Learning-Forgetting-Relearning-Forgetting" behavior observed in human brains. As illustrated in Fig. 2j, a series of five uniform light pulse trains was applied to stimulate the devices. The EPSC demonstrates notable potentiation during the first pulse, corresponding to the "Learning" phase, followed by a gradual decay to its baseline level during the subsequent "Forgetting" phase, which mimics the learning behavior observed in human brains. Notably, during the second stimulation, referred to as the "Relearning" phase, only three pulses were required to restore the synaptic weight, representing a substantial 60% reduction in the number of pulses compared to the initial stimulation. Furthermore, after relearning, the decay time of EPSC is extended from 0.8 to 1 s, indicating a 25% increase in decay duration. This phenomenon closely resembles an individual's ability to reacquire lost information [37–40].

Spike-timing-dependent plasticity (STDP) is a fundamental mechanism underlying long-term synaptic plasticity and serves as a prevalent rule for weight updating in spiking neuron networks [41]. According to the Hebbian STDP rule, the strength of synaptic connections can be effectively modulated by programming pulses, which encode spike timing information through the amplitude and duration of applied pulses within neuronal networks. The change in synaptic weight (ΔW), representing the connection between two neurons, depends on the relative timing (Δt) of activations from pre-synaptic and post-synaptic neurons. Specifically, when the pre-spike precedes the post-spike ($\Delta t > 0$), it results in synaptic weight enhancement. Clearly, the integration of optical and electrical stimulation in the device effectively induces STDP, a critical mechanism underlying synaptic changes associated with learning and memory. In particular, light stimulation functions as presynaptic stimuli leading to synaptic enhancement, while electrical stimulation acts as postsynaptic stimuli, result in synaptic inhibition (Fig. S3a). Additionally, the homologous suppression effect of the device under negative voltage is illustrated in Fig. S3b. In contrast, when the post-spike precedes the pre-spike ($\Delta t < 0$), it results in a reduction of synaptic strength, as evidenced by the analysis of neuron functional connections using a brain-computer interface platform. An exponential function is used to fit ΔW against relative Δt: $\Delta W = A\exp(-\Delta t/\tau)$, where A represents the scaling factor and τ denotes the time constants for positive and negative values of Δt, respectively. The calculated values for A are 33.8/−20.5, while τ is determined to be 0.28/−0.20 s for $\Delta t > 0$ and $\Delta t < 0$, respectively (as indicated by the solid line in Fig. S3c).

The dendritic nerve is a crucial component of the biological nervous system. Dendritic neurons receive neural impulses from other neurons, integrate this information, and route it for output, thereby playing a critical role in the neural activity of organisms (Fig. S3d) [42]. The importance of associative learning in the cognitive functions of biological nervous systems is highlighted by classical Pavlovian conditioning experiments [43,44]. Using SiC/SiO$_2$@Ag NWN artificial synaptic devices, the "Pavlov" conditional reflex can be effectively replicated. In these devices, the unconditioned stimulus (US), represented by a feeding pulse, and the conditioned stimulus (CS), represented by a bell pulse, are activated by a 365 nm light stimulus and a 5 V electrical stimulus, respectively (Fig. S3e). Using SiC/SiO$_2$@Ag NWN artificial synaptic devices, the "Pavlovian" conditional reflex can be effectively replicated. Upon application of a 5 V, 200 ms bell ringing CS to the SiC/SiO$_2$@Ag NWN artificial synaptic devices (synapse 1), an inferior response below the threshold value of 0.7 pA is generated, indicating no significant response. When a food pulse US (365 nm, 326 mW/cm^2, 200 ms, synapse 2) is applied, it elicits a response that exceeds the threshold value (UR), thereby demonstrating a more pronounced reaction. During the training phase, the simultaneous application of two light pulses (CS+US) results in a marked increase in the response, surpassing the UR. Following the training session, during which the bell ringing stimulus (originally CS) is applied, the synapses subsequently exhibit a conditioned response (CR) when stimulated independently, exceeding the threshold value. This demonstrates the successful achievement of Pavlovian learning through the utilization of the SiC/SiO$_2$@Ag NWN device.

Zero-bias photoexcitation mode visual synapse

The schematic diagram of the device test under 0 driving voltage for optical modulation is shown in Fig. 3a. The mechanisms underlying the synaptic performance in the light modulation mode of the SiC/SiO$_2$@Ag NW artificial synaptic devices are analyzed. When SiC/SiO$_2$/Ag NWs are exposed to 365 nm light (Fig. 3b), this energy is sufficient to excite electrons of SiC from the valence band to the conduction band, generating electron-hole pairs. Under UV light irradiation, monodispersed Ag NPs anchored on the SiC NW surface generate a strong LSPR effect due to the collective oscillation of free electrons. This phenomenon results in the generation of hot electrons through subsequent nonradiative decay processes within the Ag NPs. However, the transfer of these hot-electrons is impeded by the insulating SiO$_2$ interlayer. Despite this barrier, plasmon resonance energy transfer (PRET) and local electromagnetic field enhancement (LEMFE), facilitate the transfer of plasmon resonance energy from the Ag NPs to SiC NW. Consequently, this energy transfer enhances the optical absorption of SiC, thereby increasing the rate of inter-band transitions and promoting the formation of electron-hole pairs. The PPF can be effectively achieved using pulsed light at a wavelength of 365 nm. It is observed that the enhancement effect attenuates as the pulse

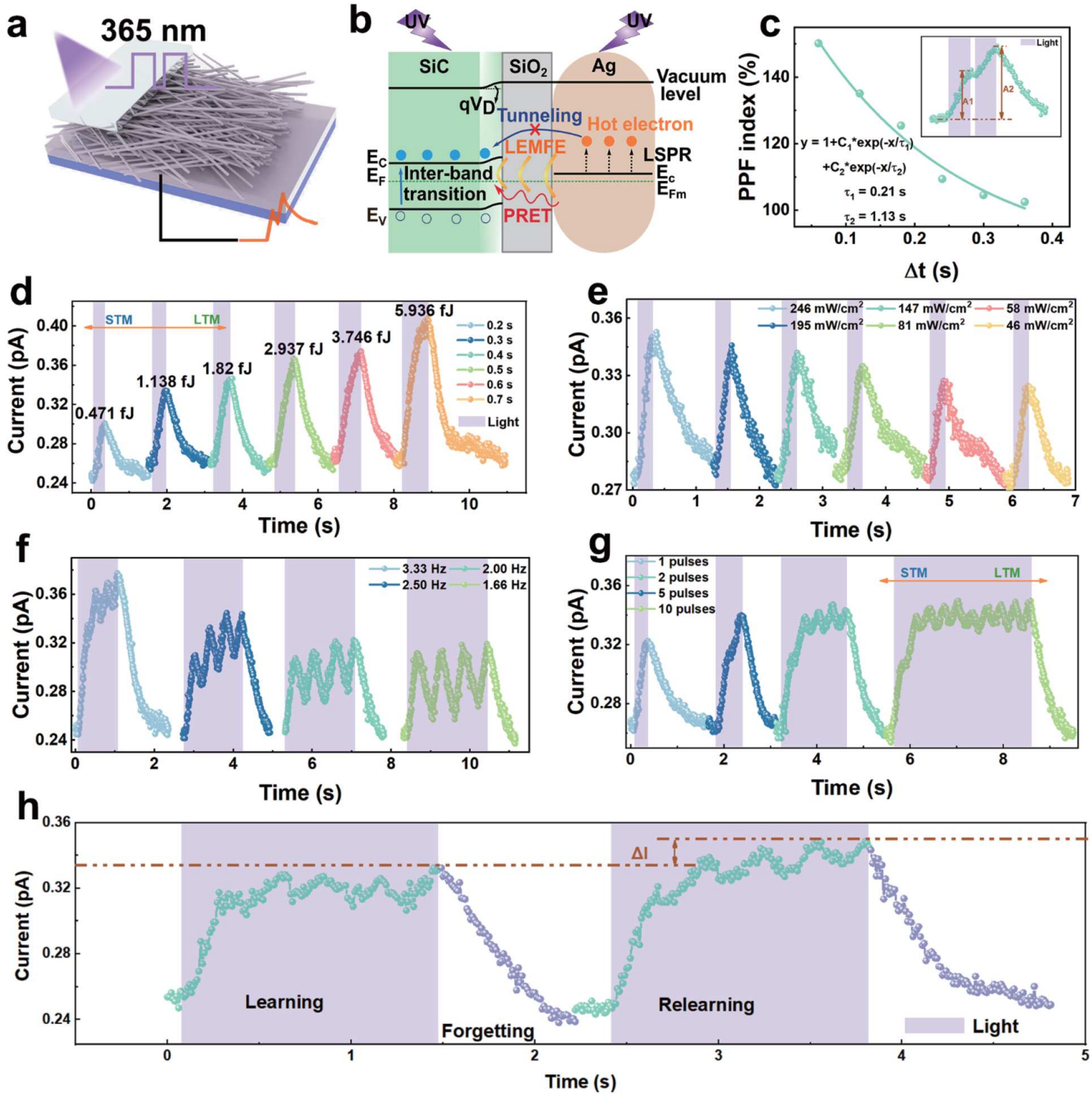

Figure 3 (a) Schematic diagram of the device's zero-bias photoexcitation mode. (b) Energy band diagram of the SiC/SiO$_2$@Ag heterojunction under 365 nm UV illumination. (c) PPF index as a function of the time interval between two light pulses: simulation test of device dissimilation during double-pulse operation. Device response to 365 nm light pulses with varying parameters: (d) pulse widths, (e) power densities, (f) pulse numbers, and (g) frequencies repeated at 10 times. (h) "Learning-Forgetting-Relearning-Forgetting" behavior exhibited by the device under light stimulation.

interval increases, consistent with the corresponding trend in biological PPF, as displayed in Fig. 3c. The experimental PPF indexes fitting analysis reveals that τ_1 and τ_2 are 0.21 and 1.13 s, respectively. It is well established that device array uniformity and long-term degradation data are critical for validating the noise immunity and feasibility of hardware-based neural networks. Fig. S4a–c evaluate the synaptic stability through PPF tests. As shown in these figures, the PPF index after six months and one year of storage exhibits minimal deviation from the initial state, indicating robust synaptic plasticity under ambient conditions. Furthermore, Fig. S5 provides additional evidence of array-level uniformity: under identical testing conditions, four independent synaptic devices exhibit PPF indices of 150.75%, 156.30%, 159.39%, and 157.25%, respectively, thereby confirming their suitability for implementation in hardware-based neural networks. As external stimuli intensify, the EPSC increases progressively with enhanced pulse width (ranging from 200 to 700 ms) (Fig. 3d), pulse amplitude (from 46 to 246 mW/cm^2) (Fig. 3e), pulse frequency (from 1.66 to 3.33 Hz) (Fig. 3f), and pulse number (from 1 to 10) (Fig. 3g). Consequently, by modulating the intensity of light stimulation intensity, the SiC/SiO$_2$@Ag device successfully transitions from STM to LTM under zero-bias photoexcitation mode. In addition, the SiC/SiO$_2$@Ag device realizes zero-bias photoexcitation mode visual synapses with extremely low power consumption. By quantifying the energy consumption of the device under different pulsed stimulation durations (Fig. 3d), it is found that the device consumes only 0.471 fJ of power under 200 ms light pulsed stimulation, a value comparable to that of human brain synapses. In comparison with other reported semiconductor optoelectronic synapses, our devices exhibit the lowest energy consumption, as summarized in Table S1 [14,33,45–51].

As the stimulation duration increased to 700 ms, the power consumption of the device is only 5.936 fJ. This enhanced performance can be attributed to the significant improvement in light response achieved by the LSPR effect generated by Ag NPs, as well as the effective management of carrier movement and reduction of losses enabled by the one-dimensional structural confinement provided by NWs. Consequently, this results in a remarkably low current state throughout the entire NW. This exceptional performance is primarily due to the synergistic effects between Ag NPs and NWs, leading to reduced power consumption levels. Moreover, the SiC/SiO$_2$@Ag NW artificial synaptic devices also present favorable "Learning-Forgetting-Relearning-Forgetting" behavior under zero-bias photoexcitation mode conditions (Fig. 3h). The EPSC during the "Relearning" process is significantly potentiated by training, with only two pulses required to achieve EPSC levels comparable to those observed during the initial "Learning" phase, despite the delay time increasing from 400 to 700 ms.

Electrically modulated synapse

It is noteworthy that the SiC/SiO$_2$@Ag NWN artificial synaptic devices exhibit synaptic behavior in response to electrical stimulation, utilizing the same structure. During testing under varying polarity voltages, the device's current output is observed to increase under positive voltages and decrease under negative ones. This finding can be employed to validate the mechanisms of synaptic enhancement and inhibition. The schematic diagram of the device test is presented in Fig. 4a. The PPF and paired-pulse depression (PPD) values for 5 and −5 V pulses are depicted in Fig. 4b and Fig. S3b, respectively. The experimental PPF indices can be described by the equation $y = 1+C_1\exp(-\Delta t/\tau_1)+C_2\exp(-\Delta t/\tau_2)$, with the fitted results represented as solid lines in Fig. 4b and Fig. S3b. The time constants τ_1 and τ_2 were determined to be 0.28 and 9.81 s, respectively. The device demonstrates an adaptive transition from STM to LTM as the intensity of external stimuli increases, concurrently exhibiting an increase in the EPSC with progressively enhanced pulse width (Fig. 4c), pulse amplitude (Fig. 4d), pulse frequency (Fig. S6a), and pulse number (Fig. S6b). The SiC/SiO$_2$@Ag device realizes electrical synaptic functionality with remarkably low power consumption. By evaluating the energy consumption of the device under varying pulsed stimulation durations (Fig. 4d), it is determined that the device consumes only 15 fJ of power under 100 ms electrical pulsed stimulation, comparable to that of a human brain synapse. When the stimulation duration is extended to 500 ms, the power consumption remains as low as 3.085 pJ. Furthermore, the SiC/SiO$_2$@Ag NW artificial synaptic devices display a pronounced "Learning-Forgetting-Relearning-Forgetting" behavior (Fig. 4e). During the "Relearning" phase, the EPSC is significantly potentiated through training, requiring only four pulses to achieve the same level as the initial "Learning" phase as the delay time increases from 700 to 900 ms. Additionally, the response speed of the device is examined by applying continuous electrical pulses through electrical stimulation.

By utilizing the enhancing effect of positive pulses and the inhibitory effect of negative pulses, along with fine-tuning the time interval between them (Fig. S7), implementation of STDP function was successfully achieved under electrical stimulation (Fig. 4f). The STDP exponential function $\Delta W = A\exp(-\Delta t/\tau)$ is employed for fitting, resulting in calculated values of A and τ as 86.5/−102.7 and 0.06/−0.04 s for $\Delta t > 0$ and $\Delta t < 0$, respectively, consistent with the classic STDP model. Furthermore, the functionality of dendrites under electrical stimulation can be emulated by interconnecting two SiC/SiO$_2$@Ag NW artificial synaptic devices (Fig. S8), thereby establishing input structures at both ends and an output structure at one end. By harnessing the dendrite function, the "Pavlov" conditioned reflex can be successfully implemented through electrical stimulation (Fig. 4g). The SiC/SiO$_2$@Ag NW artificial synaptic devices receive a bell signal (5 V pulse, synapse 1) and a food signal (10 V pulse, synapse 2). When the bell is applied to the device, the response remains below the threshold of 0.5 picoamperes. On the other hand, applying the food signal to synapse 2 triggers a response that exceeds this threshold. During the training sessions, where bell and food stimuli are sequentially administered, a significant response above the threshold is consistently observed. Consequently, in subsequent testing phases, the presentation of only the bell signal can trigger synaptic responses that exceed the threshold value, thereby demonstrating Pavlovian learning.

An in-depth analysis of the detailed mechanisms underlying the impact of electrical stimulation on synaptic function is conducted, particularly under conditions of minimal power consumption (Fig. 4h, i). As a highly reactive metal, silver readily undergoes electron transfer in response to an electric field, facilitating redox reactions that enable the SiC/SiO$_2$@Ag NWN to exhibit the atomic switching networks (ASN) functionality effectively. Upon application of a positive voltage, the Ag atoms within Ag NPs attached to SiC NWs can ionize into Ag$^+$ ions, which subsequently diffuse into adjacent SiC NWs (Fig. 4i, left). As the applied voltage increases, the Ag conduction path progressively extends until Ag atoms bridge two SiC NWs, forming interconnected nodes at their crossing points (Fig. 4i, middle). With prolonged voltage application, more NW nodes become connected, enhancing the overall connectivity of the entire NW network. This increased connectivity results in elevated current level within the device, mimicking the behavior of biological synapses. When the applied electric field is subsequently reduced, the conductive filament spontaneously breaks down, returning the device to a low current state (Fig. 4i, right) [52]. Moreover, when the polarity of the applied electric field is reversed, the conductive filament progressively dissolves as a result of silver ionization, drift, and reduction. This dissolution process causes the filament to gradually narrow until it eventually disappears, thereby switching the device back to its initial state [22,53]. Given the abundant presence of Ag NPs in the SiC/SiO$_2$@Ag NWNs (Fig. 4h), these NPs migrate exclusively between adjacent NWs, endowing SiC/SiO$_2$@Ag with ASN functionality. Due to the extremely narrow spacing between neighboring NWs, the required working voltage for filament channel formation is significantly reduced, along with a shortened duration of electric field action. Consequently, SiC/SiO$_2$@Ag NWN devices exhibit remarkably low power consumption.

Musical classification neural network system

In the realm of music information processing and artificial

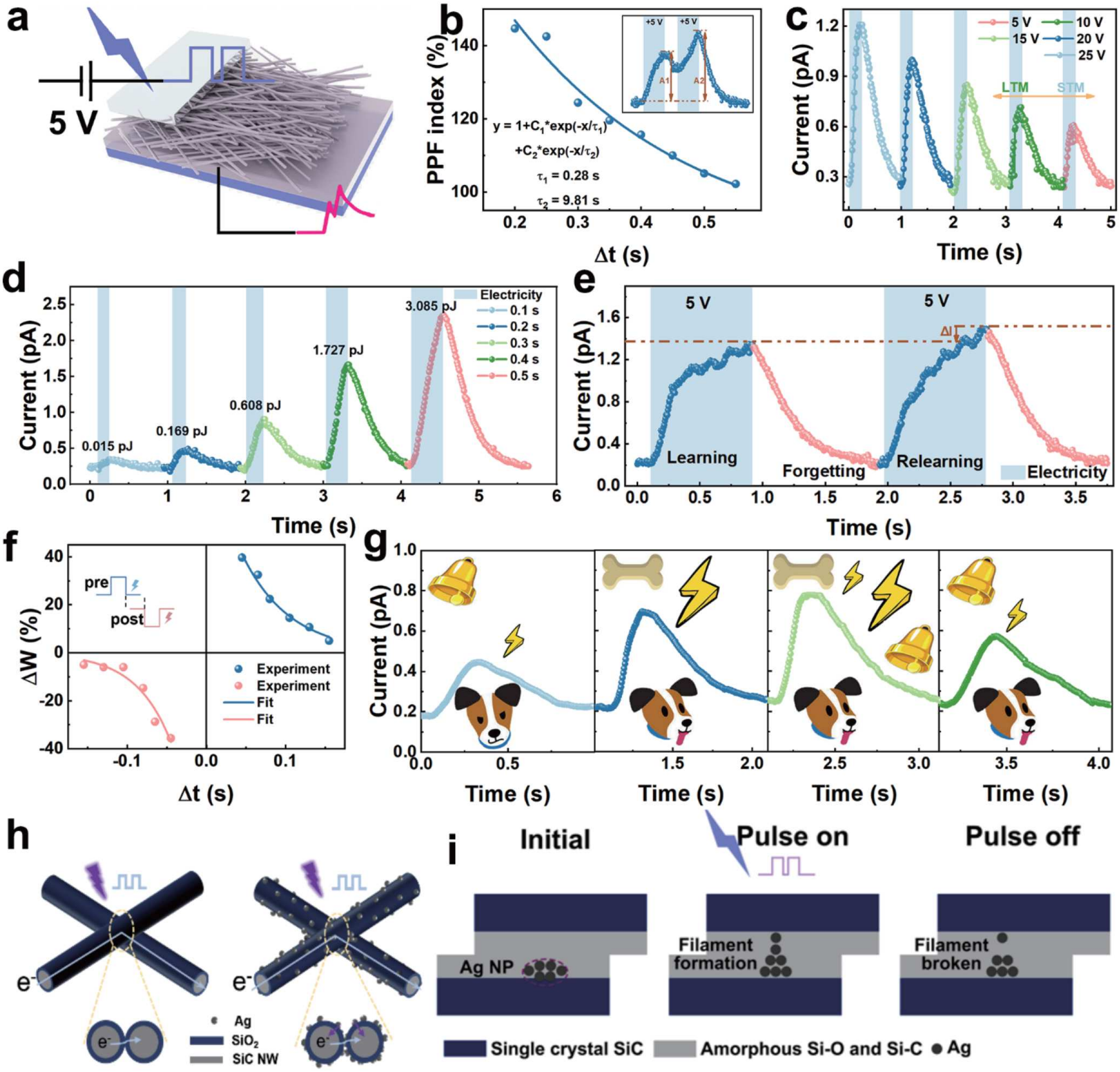

Figure 4 (a) Schematic diagram of the device electrical response testing. (b) PPF index versus time interval between two electrical pulses. Inset: simulation results of double-pulse dissimilation test for the device. (c) Device response to electrical pulses with varying amplitudes. (d) Device response to 5 V electrical pulses with different pulse widths. (e) "Learning-Forgetting-Relearning-Forgetting" behavior of the device under electrical stimulation. (f) Test results of the asymmetric Hebbian STDP protocol under electrical stimulation. (g) SiC NW artificial synapse successfully mimics Pavlov's learning with diverse electrical stimuli. (h) Electron transport characteristics in SiO$_2$-coated SiC NWs with and without the Ag NPs loading. (i) ASN phenomena between NWs in the SiC/SiO$_2$@Ag NWN device. Left: Ag NPs in their initial state; middle: Ag NPs migrating between NWs to form conductive filaments under electrical pulse stimulation; right: disruption of Ag conductive filaments following cessation of electrical pulse stimulation.

intelligence, an innovative musical note classification system has being emerged. This system effectively harnesses the STDP characteristics of low-power devices (Fig. S3c and Fig. 4f), integrating advanced hardware technology with biologically inspired learning mechanisms. Consequently, it can provide an efficient and precise solution for musical note-recognition tasks. At its core, this system combines the excellent feature extraction capabilities of traditional convolutional neural networks with the energy efficiency advantages of spiking neural networks, implementing a distinctive weight update mechanism that directly utilizes the inherent STDP properties of the hardware devices.

The system's data processing flow comprises three primary stages: the preprocessing of musical note data, the core neural network architecture, and the post-processing of network output (Fig. 5a). In the preprocessing stage, raw musical note data undergoes a series of rigorously designed procedures. First, original data are sourced from diverse sheet music or handwritten notes. Next, this data are subjected to stringent purification processes to eliminate noise and outliers that could negatively affect recognition accuracy. Specialized algorithms subsequently extract key features of the notes, such as shape,

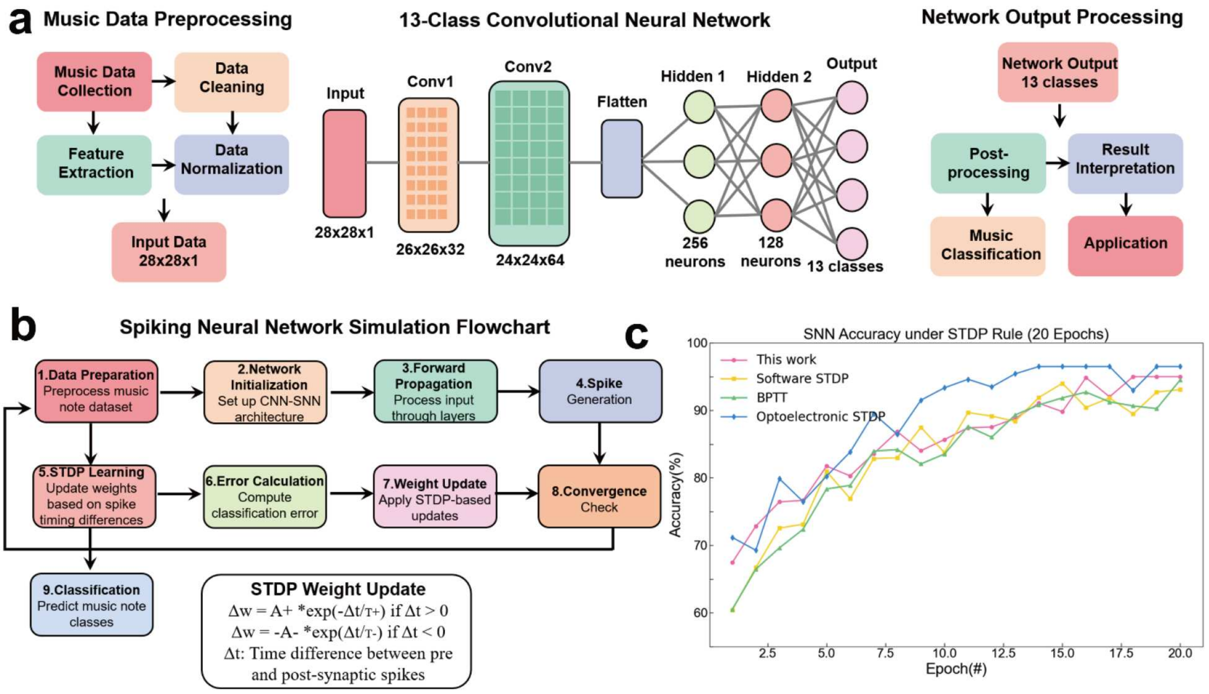

Figure 5 (a) STDP-based music classification neural network system using low-power devices. Depiction of a 13-class convolutional neural network architecture and data flow. From left to right, it showcases three main stages: music data preprocessing, neural network architecture, and network output processing. The neural network consists of two convolutional layers, a flattened layer, and two hidden layers, ultimately outputting 13 music categories. (b) Simulation flowchart for the STDP-based spiking neural network. This flowchart delineates the comprehensive process from data preparation to classification prediction, emphasizing the utilization of the STDP learning rule for synaptic weight updates. (c) Comparative analysis of SNN accuracy based on STDP rules (20 training epochs). The graph compares the classification accuracy of the STDP implementation on low-power devices with software-based STDP and back-propagation through time (BPTT) methods across different training epochs. The results indicate that the STDP implementation on low-power devices demonstrates excellent performance in later stages of training.

size, position, and orientation. These features are then normalized and transformed into standardized 28×28 pixel grayscale images, which serve as input for the neural network. This format not only retains crucial visual information of the notes but also significantly reduces computational complexity. The neural network architecture utilizes a 13-class convolutional neural network structure, enabling the system to recognize 13 distinct types of musical notes or symbols. This includes whole notes, half notes, quarter notes, eighth notes with varying time values, as well as various accidentals. The network's front end consists of two meticulously designed convolutional layers. The first layer processes the 28×28 input into a 26×26×32 feature map, capturing fundamental shapes and edge information of the musical elements. The second layer further refines this into a 24×24×64 feature map, extracting higher-level feature combinations such as the relative positional relationships between specific note components (e.g., note heads, stems).

Following the convolutional layers, a flattening layer converts the two-dimensional feature maps into one-dimensional vectors, preparing them for subsequent fully connected layers. Two hidden layers, comprising 256 and 128 neurons respectively, further process these features through abstraction and combination. The final output layer consisting 13 neurons provides the classification results. This hierarchical architecture enables the network to progressively transition from detecting simple lines and curves to recognizing complex note shapes and overall layout, thereby achieving high-precision note recognition. During the network output processing stage, raw outputs undergo post-processing, result interpretation, and practical application. Specifically, the network's digital outputs are translated into concrete musicological concepts, such as, interpreting an output as "quarter note, pitch C4". Additionally, this stage may incorporate contextual analysis, including evaluating relationships between adjacent notes to rectify potential recognition errors, or adjusting results based on the score's structure elements (e.g., bar lines, time signatures).

To quantitatively evaluate the programming accuracy and retention characteristics of weight states in SiC/SiO$_2$@Ag NW synaptic devices, we employed confusion matrix analysis (Fig. S9). The primary role of this matrix is to assess the correspondence between the target conductance states (representing the desired synaptic weights) and the experimentally measured conductance states. Crucially, the system's training process directly harnesses the STDP characteristics inherent in low-power devices. The simulation flowchart of the STDP-based spiking neural network is illustrated in Fig. 5b. This approach emulates biological neural systems, where synaptic strength adjustments are determined by the relative timing of pre- and post-synaptic neuron firings. Specifically, when a pre-synaptic neuron emits a spike shortly before the post-synaptic neuron fires, the corresponding synaptic weight is strengthened. Conversely, if the pre-synaptic spike arrives after the post-synaptic firing, the synaptic weight is depressed. By utilizing the intrinsic STDP properties of the hardware, combined with the characteristics of SiC/SiO$_2$@Ag NW synaptic devices, the system realizes this learning mechanism with greater efficiency and lower power consumption compared to traditional software-based implementations. This hardware-implemented STDP enables adaptive learning of temporal features in input stimuli, thereby significantly enhancing classification accuracy and system robustness. Results demonstrate that although the low-power device-based STDP implementation initially exhibits slightly lower performance during the early stages of training, its performance rapidly surpasses traditional software implementations and backpropagation methods as training progresses, especially after more than 10 epochs. By the end of 20 training epochs, this hardware-based STDP method achieves an accuracy approaching 95%, demonstrating superior learning ability and generalization performance (Fig. 5c). These findings not only validate the effectiveness of the proposed system but also highlight its potential for long-term training and practical applications, particularly in complex musical environments requiring continuous learning and adaptation.

CONCLUSIONS

This study demonstrates a low-power artificial synaptic device based on SiC NWNs, achieving remarkable energy efficiency (0.471–0.218 pJ per synaptic event) and high computational accuracy (>95% within 20 epochs). The device emulates both visual and electrical synaptic plasticity by modulating junctional dynamics, offering a hardware foundation for spiking neural networks. Its ultralow power consumption and scalability enable energy-efficient neuromorphic systems, particularly for robust music classification tasks requiring fault tolerance to noisy inputs. This work advances the development of bio-inspired computing architectures for next-generation intelligent music processing technologies.

Received 25 April 2025; accepted 12 June 2025;

1 Ielmini D, Wong HSP. In-memory computing with resistive switching devices. Nat Electron, 2018, 1: 333–343
2 Kendall JD, Kumar S. The building blocks of a brain-inspired computer. Appl Phys Rev, 2020, 7: 011305
3 Mehonic A, Kenyon AJ. Brain-inspired computing needs a master plan. Nature, 2022, 604: 255–260
4 Zhu Y, Mao H, Zhu Y, *et al.* CMOS-compatible neuromorphic devices for neuromorphic perception and computing: a review. Int J Extrem Manuf, 2023, 5: 042010
5 Li R, Yue Z, Luan H, *et al.* Multimodal artificial synapses for neuromorphic application. Research, 2024, 7: 0427
6 Yuan S, Feng Z, Qiu B, *et al.* Silicon carbide nanowire-based multifunctional and efficient visual synaptic devices for wireless transmission and neural network computing. Sci China Mater, 2023, 66: 3238–3250
7 Fu J, Nie C, Sun F, *et al.* Bionic visual-audio photodetectors with in-sensor perception and preprocessing. Sci Adv, 2024, 10: eadk8199
8 Liu L, Xu W, Ni Y, *et al.* Stretchable neuromorphic transistor that combines multisensing and information processing for epidermal gesture recognition. ACS Nano, 2022, 16: 2282–2291
9 Zhang W, Yao P, Gao B, *et al.* Edge learning using a fully integrated neuro-inspired memristor chip. Science, 2023, 381: 1205–1211
10 Wang W, Wang Y, Yin F, *et al.* Tailoring classical conditioning behavior in TiO_2 nanowires: ZnO QDs-based optoelectronic memristors for neuromorphic hardware. Nano-Micro Lett, 2024, 16: 133
11 Huang W, Zhang H, Tang J, *et al.* Self-powered optoelectronic synaptic devices for neuromorphic computing with the lowest energy consumption density. ACS Photonics, 2024, 11: 3095–3104
12 Islam MM, Krishnaprasad A, Dev D, *et al.* Multiwavelength optoelectronic synapse with 2D materials for mixed-color pattern recognition. ACS Nano, 2022, 16: 10188–10198
13 Weng Z, Ji T, Yu Y, *et al.* Memristive devices based on necklace-like structure Ag@TiO_2 nanowire networks for neuromorphic learning and reservoir computing. ACS Appl Nano Mater, 2024, 7: 21018–21025
14 Zhou M, Zhao Y, Gu X, *et al.* Light-stimulated low-power artificial synapse based on a single GaN nanowire for neuromorphic computing. Photon Res, 2023, 11: 1667
15 Zhang Y, Ma Z, Chen Z, *et al.* Perovskite-nanowire-array-based continuous-state programmable artificial synapse for neuromorphic computing. Adv Intelligent Syst, 2024, 6: 2300586
16 Kuncic Z, Nakayama T. Neuromorphic nanowire networks: principles, progress and future prospects for neuro-inspired information processing. Adv Phys-X, 2021, 6: 1894234
17 Diaz-Alvarez A, Higuchi R, Sanz-Leon P, *et al.* Emergent dynamics of neuromorphic nanowire networks. Sci Rep, 2019, 9: 14920
18 Loeffler A, Diaz-Alvarez A, Zhu R, *et al.* Neuromorphic learning, working memory, and metaplasticity in nanowire networks. Sci Adv, 2023, 9: eadg3289
19 Hochstetter J, Zhu R, Loeffler A, *et al.* Avalanches and edge-of-chaos learning in neuromorphic nanowire networks. Nat Commun, 2021, 12: 4008
20 Chong H, Yang H, Yang W, *et al.* SiC nanowire film photodetectors: a promising candidate toward high temperature photodetectors. J Nanosci Nanotechnol, 2016, 16: 3796–3801
21 Qin H, Sun S, He N, *et al.* Wide-bandgap semiconductor SiC-based memristors fabricated entirely by electron beam evaporation for artificial synapses. Appl Phys Lett, 2024, 125: 143502
22 Liu L, Zhao J, Cao G, *et al.* A memristor-based silicon carbide for artificial nociceptor and neuromorphic computing. Adv Mater Technologies, 2021, 6: 2100373
23 Lu M, Zhai P, Li L, *et al.* Transferable 3C-SiC nanowire network film for high performance flexible UV photodetectors with a simple, low cost and large scale production. Sens Actuat A-Phys, 2023, 363: 114741
24 Zirakjou A, Kokabi M. SiC/C aerogels from biphenylene-bridged polysilsesquioxane/clay mineral nanocomposite aerogels. Ceramics Int, 2020, 46: 2194–2205
25 Chen M, Tang Z, Liu H, *et al.* High-performance single SiC nanocable-based plasmonic photodetectors for ultraviolet communication systems. Mater Today Nano, 2025, 29: 100544
26 Hallin C, Konstantinov AO, Pécz B, *et al.* The origin of 3C polytype inclusions in epitaxial layers of silicon carbide grown by chemical vapour deposition. Diamond Relat Mater, 1997, 6: 1297–1300
27 Seong HK, Choi HJ, Lee SK, *et al.* Optical and electrical transport properties in silicon carbide nanowires. Appl Phys Lett, 2004, 85: 1256–1258
28 Chih B, Engelman H, Scheiffele P. Control of excitatory and inhibitory synapse formation by neuroligins. Science, 2005, 307: 1324–1328
29 Qin S, Wang F, Liu Y, *et al.* A light-stimulated synaptic device based on graphene hybrid phototransistor. 2D Mater, 2017, 4: 035022
30 Son DI, Park DH, Choi WK, *et al.* Carrier transport in flexible organic bistable devices of ZnO nanoparticles embedded in an insulating poly(methyl methacrylate) polymer layer. Nanotechnology, 2009, 20: 195203
31 Wang Z, Joshi S, Savel'ev SE, *et al.* Memristors with diffusive dynamics as synaptic emulators for neuromorphic computing. Nat Mater, 2017, 16: 101–108
32 Kumar M, Ban D, Kim SM, *et al.* Vertically aligned WS_2 layers for high-performing memristors and artificial synapses. Adv Elect Mater, 2019, 5: 1900467
33 Zhou M, Zhao Y, Gu X, *et al.* Realize low-power artificial photonic synapse based on (Al,Ga)N nanowire/graphene heterojunction for neuromorphic computing. APL Photonics, 2023, 8: 076107
34 Li JF, Zhang YJ, Ding SY, *et al.* Core–shell nanoparticle-enhanced raman spectroscopy. Chem Rev, 2017, 117: 5002–5069
35 Yang M, Zhao X, Tang Q, *et al.* Stretchable and conformable synapse memristors for wearable and implantable electronics. Nanoscale, 2018, 10: 18135–18144
36 Hwang H, Woo J, Lee T, *et al.* Synaptic plasticity and preliminary-spike-enhanced plasticity in a CMOS-compatible Ta_2O_5 memristor. Mater Des, 2020, 187: 108400

37 Chang T, Jo SH, Lu W. Short-term memory to long-term memory transition in a nanoscale memristor. ACS Nano, 2011, 5: 7669–7676

38 Wang ZQ, Xu HY, Li XH, *et al.* Synaptic learning and memory functions achieved using oxygen ion migration/diffusion in an amorphous InGaZnO memristor. Adv Funct Mater, 2012, 22: 2759–2765

39 He H, Yang R, Zhou W, *et al.* Photonic potentiation and electric habituation in ultrathin memristive synapses based on monolayer MoS_2. Small, 2018, 14: 1800079

40 Liu G, Wang C, Zhang W, *et al.* Organic biomimicking memristor for information storage and processing applications. Adv Elect Mater, 2016, 2: 1500298

41 Zhao J, Liu F, Huang Q, *et al.* Charge trap-based carbon nanotube transistor for synaptic function mimicking. Nano Res, 2021, 14: 4258–4263

42 London M, Häusser M. Dendritic computation. Annu Rev Neurosci, 2005, 28: 503–532

43 Crow T. Pavlovian conditioning of *Hermissenda*: current cellular, molecular, and circuit perspectives. Learn Mem, 2004, 11: 229–238

44 Moon K, Park S, Jang J, *et al.* Hardware implementation of associative memory characteristics with analogue-type resistive-switching device. Nanotechnology, 2014, 25: 495204

45 Yin L, Han C, Zhang Q, *et al.* Synaptic silicon-nanocrystal phototransistors for neuromorphic computing. Nano Energy, 2019, 63: 103859

46 Mo Y, Luo B, Dong H, *et al.* Light-stimulated artificial synapses based on Si-doped GaN thin films. J Mater Chem C, 2022, 10: 13099–13106

47 Shen R, Jiang Y, Li X, *et al.* Artificial synapse based on an InAs nanowire field-effect transistor with ferroelectric polymer P(VDF-TrFE) passivation. ACS Appl Electron Mater, 2022, 4: 5008–5016

48 Gu X, Zhou M, Zhao Y, *et al.* Realize ultralow-energy-consumption photo-synaptic device based on a single (Al,Ga)N nanowire for neuromorphic computing. Nano Res, 2023, 17: 1933–1941

49 Yan X, Jia X, Zhang Y, *et al.* A low-power Si:HfO_2 ferroelectric tunnel memristor for spiking neural networks. Nano Energy, 2023, 107: 108091

50 Wang T, Meng J, Zhou X, *et al.* Reconfigurable neuromorphic memristor network for ultralow-power smart textile electronics. Nat Commun, 2022, 13: 7432

51 Zhu M, Yu Z, Hu G, *et al.* A TaO_x/TiO_y bilayer memristor with enhanced synaptic features for neuromorphic computing. Adv Elect Mater, 2024, 10: 2400008

52 Ham S, Choi S, Cho H, *et al.* Photonic organolead halide perovskite artificial synapse capable of accelerated learning at low power inspired by dopamine-facilitated synaptic activity. Adv Funct Mater, 2018, 29: 1806646

53 Zhao J, Zhou Z, Zhang Y, *et al.* An electronic synapse memristor device with conductance linearity using quantized conduction for neuroinspired computing. J Mater Chem C, 2019, 7: 1298–1306

Acknowledgement This work was supported by the National Natural Science Foundation of China (11875032), Natural Science Foundation of Shaanxi Province (2023-JC-QN-0268), Shaanxi Fundamental Science Research Project for Mathematics and Physics (23JSQ004), Shaanxi Provincial Department of Education (23JK0341), Foundations of Shaanxi Province (2023-JC-YB-022), and Shaanxi Fundamental Science Research Project for Mathematics and Physics (22JSQ006). We would like to express our gratitude to Dr. Zhe Feng and Prof. Zuheng Wu for their invaluable assistance in data analysis, artificial intelligence computation, and related analytical tasks.

Author contributions The manuscript was written through contributions of all authors. Chen M carried out the experiments, analyzed the data, plotted and wrote the draft of the manuscript. Wei G contributed to the writing of the manuscript and analyzing the data. Yuan S contributed to writing of theory section of manuscript and modifying the manuscript. Wang P made changes to the manuscript. Su Y was participated in some experiments. Ding L supported experimental research. Wang R and Li Y made changes to the manuscript. Shen G supervised experiments analysis and contributed to writing of the final manuscript. All authors have given approval to the final version of the manuscript.

Conflict of interest The authors declare that they have no conflict of interest.

Supplementary information Supplementary materials are available in the online version of the paper.

Mi Chen is a PhD student at Shaanxi University of Science and Technology under the supervision of Prof. Guodong Wei. Her research mainly focuses on SiC nanomaterials for memristor applications.

Guodong Wei received his PhD degree in the physical electronics from Jilin University in 2009. He joined Shaanxi University of Science and Technology in 2020. His research interests are mainly in micro/nano fabrication and their optoelectronic device.

Guozhen Shen received his PhD degree in 2003 from the University of Science and Technology of China. He joined the Institute of Semiconductors, Chinese Academy of Sciences as a professor in 2013. His research focuses on flexible electronics and printable electronics, including transistors, photodetectors, sensors and flexible energy-storage devices.

基于低功耗等离子体SiC纳米线网络的音乐分类神经网络人工光突触器件的研究

陈咪[1], 尉国栋[1*], 袁帅[1,3], 李营[2], 王盼[1], 苏莹[1], 丁利苹[1], 王瑞红[1], 沈国震[2*]

摘要 人工智能与物联网的快速发展, 对具备高并行处理能力的类脑计算系统提出了迫切需求. 然而, 当前报道的大多数人工突触器件的功耗仍显著高于生物突触(单次突触事件功耗仅飞焦耳量级). 为此, 本研究致力于开发基于碳化硅(SiC)等离子激元纳米线网络的超低功耗的类人工突触器件, 并将其应用于音乐分类神经网络系统. 通过利用纳米线网络的类神经网络物理结构及其交叉节点处的电导态调控性质, 所制备的SiC/SiO_2@Ag纳米线网络器件在两种工作模式下, (1) 外置偏压电场调控模式, (2) 零偏置光激发模式, 成功实现了紫外光视觉与电学突触功能的模拟. 此外, 得益于一维纳米材料的限域效应及银纳米颗粒诱导的局域表面等离子体共振效应, 该器件在极低电流下表现出显著的突触响应特性, 且功耗极低. 凭借其卓越的低功耗性能, SiC/SiO_2@Ag纳米线网络突触在模拟音乐分类识别任务中表现出优异性能, 在仅20个训练周期内准确率超过95%. 值得注意的是, 创新性的SiC纳米线网络结构不仅确保了高稳健的突触性能, 还实现了高精度的神经网络计算, 这一进展有望推动脉冲神经网络等新型计算架构的发展. 这种新颖的纳米线网络架构更贴近生物神经网络的工作原理, 从而为音乐信息处理提供了更为高效的解决方案.